



Novel test section for homogeneous nucleation studies in a pulse expansion wave tube: experimental verification and gasdynamic 2D numerical model

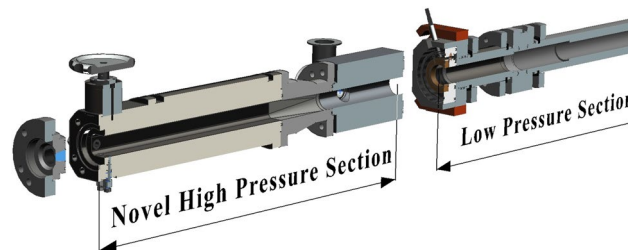
M. M. Campagna¹ · M. E. H. van Dongen² · D. M. J. Smeulders¹

Received: 28 October 2019 / Revised: 22 January 2020 / Accepted: 16 March 2020 / Published online: 27 March 2020
© The Author(s) 2020

Abstract

A novel design of a pulse expansion wave tube (PEWT) for the study of homogeneous nucleation in mixtures of vapours and gases is presented. The main difference with the previous design consists in a test section with flat walls, which avoid that optical windows and pressure transducers do affect the flow field locally. Additionally, the test section length is reduced by a factor two. The performance of the wave tube is investigated both experimentally and numerically. The thermal insulation of the piezoelectric pressure sensor is proved to be beneficial for accurate measurements. The smallest thickness possible of the diaphragm, initially separating the high- and low-pressure sections of the PEWT, is also shown to be crucial. The flow phenomena are simulated with a 2D numerical model. It is shown to correctly predict the gasdynamic features of the PEWT and the effects of the diaphragm opening process. Nucleation rates for water in helium are determined as a function of supersaturation for two different pressure conditions, 1 MPa and 0.1 MPa, at a temperature of 240 K. The good agreement with results from previous experiments shows that the geometrical mismatch of optical windows and pressure transducers in the original wave tube did not affect the nucleation rates significantly and that both the original and the new wave tube produce reliable measurement data.

Graphic abstract



1 Introduction

Condensation has been actively studied for several decades, but, nevertheless, it remains an active research area with critical implications for many industrial and environmental applications. CO₂ emission and industrial pollution are just two fields in which a profound knowledge of such phase transition plays a crucial role. Effects of condensation are also present in chemical reactors, aircraft, turbines and engine applications (Wyslouzil and Wölk 2016). The oil and gas industry is another important sector interested in condensation phenomena mainly for performance

✉ M. M. Campagna
M.M.Campagna@tue.nl

¹ Department of Mechanical Engineering, Eindhoven University of Technology, P.O. Box 513, 5600 MB Eindhoven, The Netherlands

² Department of Applied Physics, Eindhoven University of Technology, P.O. Box 513, 5600 MB Eindhoven, The Netherlands

prediction and design improvement of natural gas impurity separators (Kalikmanov et al. 2007), or even for the development of integrated devices to couple the removal of contaminants with the gas liquefaction process. Hence, a full comprehension of this phase transition and more accurate models would lead to beneficial consequences in a wide range of scientific and technological fields. A large variety of measurement techniques was applied in the past (Wyslouzil and Wölk 2016), not only to verify and validate the theory, but also to elaborate corrections for the existing condensation models. The *pulse expansion wave tube* (PEWT) is one of the expansion based devices. Initially designed to cope with the lack of experimental data related to *homogeneous condensation* of hydrocarbons, it has been largely and effectively used with water as condensing vapour at a later time. In this paper, we discuss a new PEWT measurement section with flat inner walls to allow a perfectly flush installation of optical windows and pressure sensors. As the rest of the tube remains cylindrical, a square-shape cross-over section is installed as well. Results of first wave experiments with the new gasdynamic facility will be presented including nucleation rate data for water–helium mixtures. Two-dimensional numerical simulations will be compared with experimental wave tube observations.

2 PEWT working principle

Water condensation is considered *homogeneous* when the vapour-to-liquid transition takes place in the absence of macroscopic surfaces or foreign particles. In heterogeneous condensation, such surfaces or particles act as starting points for the phase transition and a *vapour pressure* p_v slightly above the *saturated vapour pressure* p_s is sufficient to trigger the vapour-to-liquid transition. If such surfaces or impurity particles are absent, a gas–vapour mixture can easily become oversaturated ($p_v > p_s$). Nevertheless, due to the stochastic nature of the gas and the vapour molecules, clusters are formed. While the smallest ones dissolve, the largest clusters reach the so-called *critical size* n^* if adequate supersaturated conditions are met. After that, the *critical clusters* become stable droplets and grow by collision with the free vapour molecules. The process of critical cluster formation is known as *homogeneous nucleation*, and it is followed by *droplet growth*. The number of critical clusters formed per units of volume and time is defined as the *nucleation rate* J ($\text{m}^{-3}\text{s}^{-1}$). The *critical size* n^* stands for the number of molecules constituting a *critical cluster*. A key parameter in nucleation research is the supersaturation S . Its general definition is given in Appendix. Two specific cases are very useful. For an ideal vapour–gas mixture, S becomes:

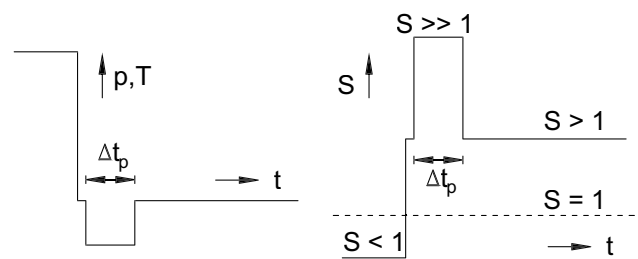


Fig. 1 Nucleation pulse method: schematic of pressure (p), temperature (T), supersaturation (S) and nucleation rate (J) in time

$$S = \frac{p_v(T)}{p_s(p, T)}. \quad (1)$$

For a dilute non-ideal vapour–gas mixture, S can be written as:

$$S = \frac{y(T)}{y_{\text{eq}}(p, T)} \quad (2)$$

with y the molar vapour fraction.

As shown by experimental evidence and confirmed by the *Classical Nucleation Theory* (Vehkamäki 2006), the nucleation rate has a strong dependency on supersaturation ratio and temperature $J(S, T)$. Exploiting such dependency, the *nucleation pulse method* (Allard and Kassner 1965) is capable of separating in time the processes of *nucleation* and *droplet growth*, enabling an accurate determination of the nucleation rate. The working principle is sketched in Fig. 1.

The initially undersaturated ($S < 1$) vapour–gas mixture is first adiabatically expanded. The corresponding temperature drop causes the saturation level to increase far above unity ($S \gg 1$). This is due to the fact that, in the case of homogeneous condensation, the partial vapour pressure p_v decreases with temperature much less than the saturated vapour pressure p_s . This state is maintained for a short time, the *nucleation pulse*, indicated in Fig. 1 with Δt_p . The supersaturation level for the pulse is chosen such that an appreciable amount of critical nuclei is formed. At the end of the pulse, the mixture is slightly recompressed, inhibiting the nucleation process to continue, but still keeping a supersaturated level ($S > 1$) for a relatively long period of time, in which the droplets can grow. In order to narrow the size distribution of the clusters, Δt_p must be kept much shorter than the growth time interval. In this way, nucleation and droplet growth are effectively decoupled and the clusters can be assumed to be approximately monodispersed (Peters 1983).

The first application of the *nucleation pulse method* dates back to 1965, when Allard and Kassner designed a piston expansion chamber to expand and recompress the test mixture, with a pulse duration of 10 ms. In order to limit vapour

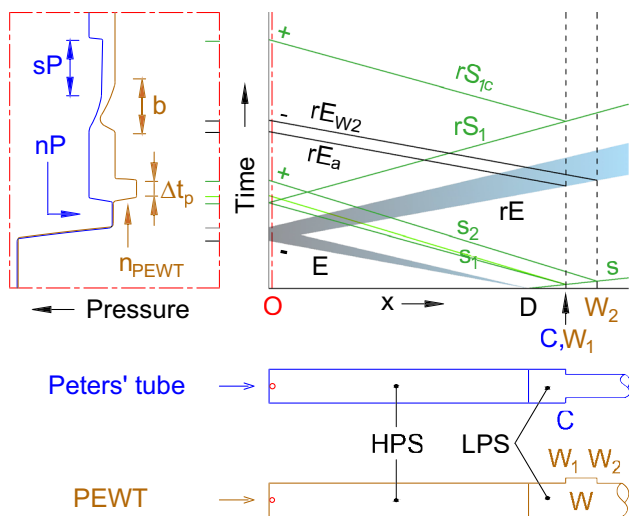


Fig. 2 Schematic $x-t$ wave diagram for the Peters' tube and the PEWT of Looijmans et al. The waves related to the expansion E are drawn in black (—), while the waves due to the shock S are represented in green (—). The resulting pressure–time profiles at the observation point O are sketched in the red box (---) on the left side of the wave diagram for both the Peter' tube (—) and the PEWT (—). Below the wave diagram, the geometrical configuration of both tubes is also represented. The observation point O is situated at few mm from the end-wall of the HPS. The length of the HPS for the PEWT of Looijmans et al. is about 125 cm, the distance between D and W_1 is about 18 cm, and the widening (W) length is 15 cm. The diameter of the tube is 36 mm, while the widening diameter is 41 mm. For comparison purposes, the Peters' tube is represented here with the same dimensions of the PEWT, but with a LPS diameter of 31 mm starting from C

depletion, polydispersity and the effect of heat released by the nucleating clusters, it is of fundamental importance to have a sufficiently short pulse duration. Therefore, Wagner and Strey (1981) later improved the design of Allard and Kassner, with a two-piston cloud chamber and a 1 ms nucleation pulse. Peters (1983) was the first to implement the *nucleation pulse principle* in a gasdynamic facility: the wave tube. The Peters' tube consists of two sections, the high pressure (*driver section*—HPS) and the low pressure (*driven section*—LPS), separated by a diaphragm. A schematic of the Peters' tube and its corresponding wave diagram is sketched in Fig. 2. After the diaphragm rupture, waves are generated: an expansion fan (E) moving towards the end wall of the HPS and a shock wave (S) in the opposite direction. The idea of Peters was to partially reflect the shock into the HPS, by reducing the LPS cross-sectional area, at position C just a few centimetres behind the diaphragm position D . Doing that, the test mixture at the observation point O is first subjected to an adiabatic expansion E . After a short time interval (Δt_p), the shock reflected at the cross-section reduction C reaches the observation point O as a weak shock wave S_1 . In this way, the mixture undergoes a slight, but

sudden, recompression and the nucleation pulse nP ends. The mixture remains at constant pressure, coinciding with the droplet growth stage. The downside of such setup was that E and S_1 , reflected at the HPS end wall as rE and rS_{1c} respectively, interact with the cross-section reduction C , generating a second slight expansion rE_a and a second weak shock rS_1 . This may lead to a second nucleation stage (sP) at the observation point O , simultaneously with the droplet growth process.

The PEWT is a modified version of the Peters' wave tube by Looijmans et al. (1993). The difference with the Peters' tube consisted in the elimination of the second nucleation pulse by replacing the cross-sectional area reduction C with a local widening W . In Fig. 2 the PEWT configuration and the corresponding wave diagram are also sketched for comparison with the Peters' tube. The modifications of Looijmans et al. implied a different way for the shock S to be reflected towards the observation point: at the enlargement W_1 as a weak expansion fan S_1 , at the restriction W_2 as a weak shock S_2 . The outcome was an isolated well-defined nucleation pulse n_{PEWT} . The end-wall reflected waves interact with the cross-sectional area change also in the PEWT case, with the difference that, beside a small recompression rE_a , also a second weak expansion rE_{W2} at W_2 is generated because of rE . Nevertheless, no appreciable disturbance on the droplet growth process is present in this case, since the interference consists of a small positive pressure ripple b after the nucleation pulse. In this way, the resulting PEWT pressure–time profile at the observation point approximates the one prescribed by the nucleation pulse method (Fig. 1) and the decoupling of the nucleation and the droplet growth processes is achieved. Once the droplets grow to a detectable size, they can be measured by optical means (details in Sect. 3).

3 Experimental methodology

The PEWT overall facility consists of 3 main parts (see Fig. 3): the Mixture Preparation device MPD (Hrubý 1999), the pulse expansion wave tube PEWT, and the Optical Setup. The experimental procedure starts with the PEWT evacuation. The HPS and the LPS are kept separated by means of a polyester (PET) diaphragm placed at the section D . Six possible diaphragm thicknesses ranging from 30 to 250 μm are available. The chosen diaphragm thickness depends on the initial pressure difference between the two sides of the PEWT. The vapour–gas mixture is prepared in the MPD sketched Fig. 3. The pure gas inside the gas bottle G_1 flows inside the MPD, where it is split into two molar flow rates Q_1 and Q_2 . The latter remains dry, while Q_1 is saturated with the pure water contained inside two saturators S_1 and S_2 . Before exiting the MPD, the fully saturated

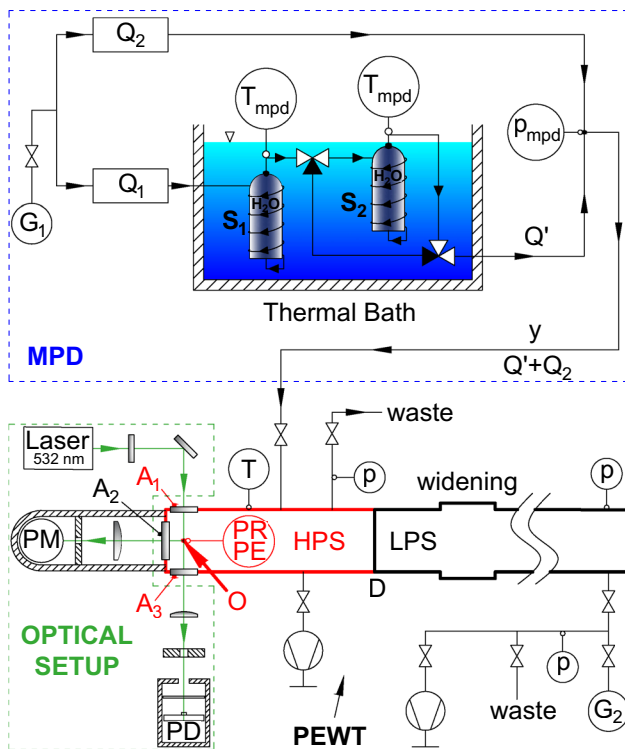


Fig. 3 Layout of the PEWT facility: the test section, the observation point *O* and the flush mounted optical windows (*A*₁, *A*₂) and pressure transducers (PR, PE) are the modified parts of the new HPS (—)

flow Q' ($Q' = Q_1 + Q_{H_2O}$) and the dry one Q_2 are mixed together. In this way, the mixture composition can be easily controlled by regulating Q_1 and Q_2 and by keeping constant the temperature T_{mpd} and the pressure p_{mpd} inside the MPD at known values. After that, the HPS is filled with the prepared mixture, while the LPS is pressurized with the pure gas contained into the gas bottle G_2 . Once the desired pressure levels are reached in both PEWT sides, the so-called *flushing procedure* starts. In this stage, the pressure level inside the HPS is kept constant and saturation of the tube walls takes place. Such procedure ends when no more net PEWT wall adsorption is present. Doing that, the mixture composition at the test section can be easily derived by calculating $y = y(Q_1, Q_2, T_{mpd}, p_{mpd})$.

Once the wall saturation condition is reached, the driver section is isolated from the MPD and the wave experiment can be run. It starts with the fast opening of the diaphragm separating the HPS from the LPS, which leads to the wave pattern described in Sect. 2 and sketched in Fig. 2. The concept and design of the diaphragm section *D* was first introduced by Looijmans and van Dongen (1997). The present configuration is shown in Fig. 4. The fast opening is triggered by an electrical pulse (200–300 A in 60–80 ms) through a Kanthal ribbon (150 × 1.75 × 0.2 mm) positioned in a circumferential groove placed at the section *D*. The

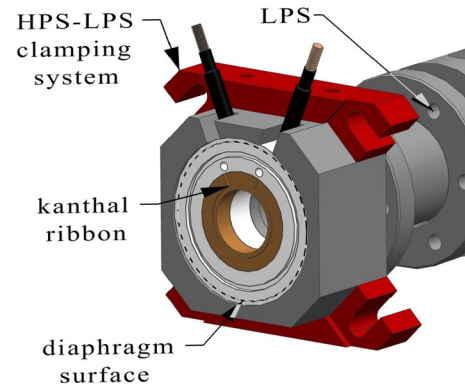


Fig. 4 3D view of the PEWT diaphragm section (*D*)

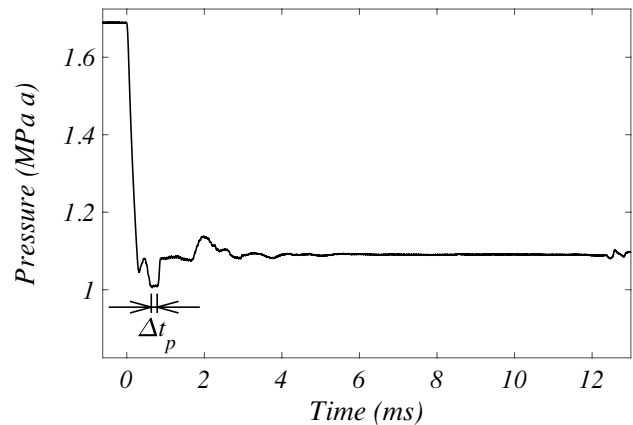


Fig. 5 Test 1 (see Table 2): PE absolute pressure–time signal

PET diaphragm remains in contact with the 0.2 mm side of the ribbon for the entire experimental procedure, being the LPS clamped to the HPS. The electrical pulse, increasing the Kanthal temperature to about 800 K, weakens the diaphragm, enabling the pressure difference to open it in a short time frame ($\sim 180 \mu s$, see Sect. 5.1). It should be noted that the ribbon does not go all the way around the entire diaphragm circumference. At the top, a few millimetres are not wired. There the PET material will remain intact, thus creating a hinge for the diaphragm to rotate around.

After the diaphragm rupture, the absolute pressure at the observation point *O* is shown in Fig. 5. The pressure is measured by means of two transducers, one piezoresistive (PR, Kistler 4073A50) and one piezoelectric (PE, Kistler 603B), placed at the test section wall. Details on the combined PR-PE measuring methodology can be found in Holten et al. (2005). By using such measuring methodology, the uncertainty on the nucleation pulse pressure is less than 0.2%. Although the PE transducer is specifically suited for measuring rapid pressure variations, as in the case of the *nucleation pulse technique*, the sensor used suffers from a

lack of thermal compensation when a temperature gradient is applied to it. Therefore, a coating layer (Dow Corning 732 black sealant) of half a millimetre has been applied to the PE sensing surface in order to insulate it from heat flow from the wall to the expanding gas. In this work, the effect of such coating on the performances of the PE transducer is object of analysis: wave experiments with dry helium have been performed to investigate the contribution of the PE transducer with and without coating layer. The temperature profile is derived from the pressure signal assuming adiabatic conditions (Looijmans and van Dongen 1997). The initial temperature of the mixture is assumed equal to the test section wall temperature, which is measured via two independent thermocouples (Tempcontrol PT-8316) with an accuracy of ± 0.03 K (Fransen et al. 2015).

Once the experimental pressure and temperature signals in time are known, it is possible to derive the pulse duration Δt_p . The corresponding supersaturation S follows from Eq. 2, with y the initial molar vapour fraction from the MPD and $y_{eq} = y_{eq}(p, T)$ the equilibrium molar vapour fraction calculated at the pulse conditions.

Knowing that the experimental form of the nucleation rate is given by the equation

$$J = \frac{n_d}{\Delta t_p}, \tag{3}$$

J can be determined if the droplet number density n_d is measured, since Δt_p is already known (Fig. 5).

In order to measure n_d , the test section is equipped with the *Optical Setup* sketched in Fig. 3, based on the light scattering and the light beam attenuation. It consists of

- a linearly polarized 100:1 laser (Lasos Lasnova GLK 3220 T01—wavelength $\lambda = 532$ nm) probing the test section through the optical window A_1 (see Fig. 3),
- a photomultiplier PM (Hamamatsu 1P28A) recording the 90° scattered irradiance $I_{sca}(t)$ at the optical window A_2 (see Fig. 3),
- a photodiode PD (Telefunken BPW 34) measuring the transmitted laser light $I(t)$ leaving the test section from the optical window A_3 (see Fig. 3).

A_1 , A_2 and A_3 are three BK7 glass windows. The laser beam interacts with the nearly monodispersed cloud of droplets generated during the nucleation pulse. As the droplets start to grow to an optically detectable size, $I_{sca}(t)$ and $I(t)$ are detected by the PM and the PD, respectively. During the growth process, $I_{sca}(t)$ shows a characteristic peaks and valleys pattern of increasing intensity in time (see Fig. 6a). Such pattern is strictly related to the droplet radius $r(t)$ for a fixed refractive index m of the medium and wavelength λ of the laser light. Simultaneously, as r grows in time, $I(t)$ is

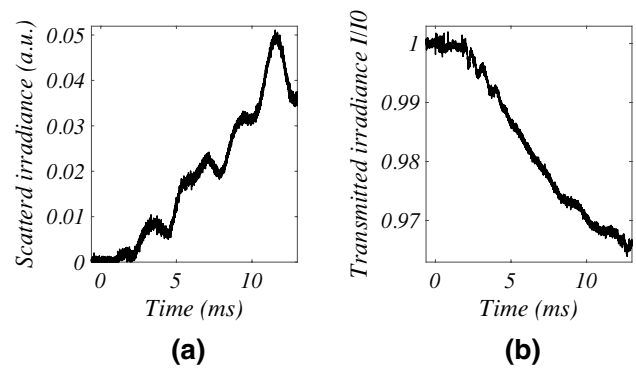


Fig. 6 Test 1 (Table 2): PM 90° scattered light–time signal (a) and PD relative transmitted light–time signal (b)

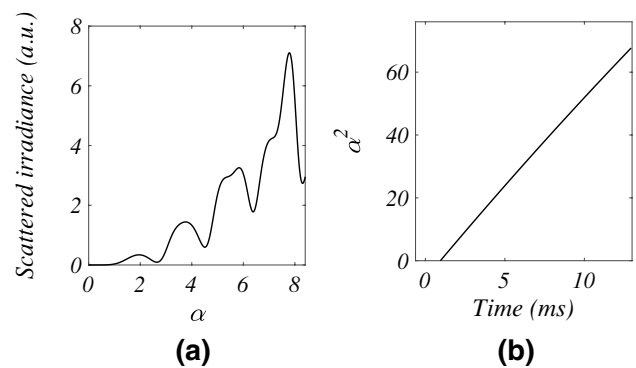


Fig. 7 Test 1 (Table 2): a theoretical 90° Mie scattered intensity as a function of the non-dimensional droplet radius $\alpha = 2\pi r/\lambda$ for a refractive index $m = 1.33$ and a wavelength $\lambda = 532$ nm; b non-dimensional droplet growth rate curve $\alpha^2(t)$ obtained by comparing the experimental $I_{sca}(t)$ in Fig. 6a with the theoretical $I_{sca,th}(\alpha)$ in Fig. 7a

attenuated proportionally to size and number density of the droplets. In Fig. 6b, a typical attenuated transmitted light $I(t)/I_0$ is shown, with I_0 the initial undisturbed value of $I(t)$.

The PM output is compared with the theoretical 90° Mie scattered intensity $I_{sca,th}(\alpha)$, which is function of the non-dimensional droplet radius $\alpha = 2\pi r/\lambda$ at a fixed λ and m . The $I_{sca,th}(\alpha)$ pattern for $\lambda = 532$ nm and $m = 1.33$ is shown in Fig. 7a. The almost one-to-one correspondence between experimental (Fig. 6a) and theoretical (Fig. 7a) scatter qualitatively proves that the assumption of nearly monodispersed droplets is well posed for the new PEWT¹ (Wagner

¹ A quantitative estimate for the variation of the droplet size within the cloud is found as follows. A droplet formed at time t_0 within the pulse period Δt_p grows according to r^2 proportional to $(t - t_0)$ as illustrated in Fig. 7b for diffusion dominated growth. Then, the width of the size distribution function is directly related to the possible variation in t_0 , which is Δt_p : $\Delta r^2/r^2 = \Delta t_p/(t - t_0)$. For $\Delta t_p = 0.2$ ms and an average growth time of 6 ms, we find for the relative width: $\Delta r/r = 0.02$.

and Strey 1981; Wagner 1985; Strey et al. 1994). Therefore, by comparing $I_{sca}(t)$ in Fig. 6a with the theoretical $I_{sca,th}(\alpha)$ in Fig. 7a, the non-dimensional droplet growth rate $\alpha^2(t)$ in Fig. 7b can be obtained.

The n_d determination follows from the Lambert–Beer law

$$\frac{I}{I_0} = e^{-n_d \pi r^2 Q_{ext} l}, \tag{4}$$

with the α -dependent terms expressed in function of time by means of the calculated $\alpha^2(t)$. The parameter l stands for the extinction length, and it is taken equal to the inner diameter of the test section (~ 32 mm for the new HPS, see Figs. 9 and 10). The extinction efficiency term $Q_{ext}(\alpha)$ can be found in the literature and is a function of the non-dimensional droplet radius α for fixed refractive indices m and wavelengths λ . The reader is referred to Fransen et al. (2014) for a detailed description of this procedure.

3.1 The newly designed HPS

A wide range of experimental conditions, accurate measurements of nucleation rates, droplet growth rates and supersaturation have made the PEWT technique a powerful tool for homogeneous condensation studies. Nucleation rate data have been determined for a wide range of pressures (0.1–4 MPa) and temperatures (220–260 K) and for different binary and ternary vapour–gas mixtures. The nucleation rates have a strong dependence on temperature, pressure and measured optical signals. In the previous version of the PEWT, a slight geometrical mismatch between the cylindrical test section wall and the flat surfaces of A_1 , A_3 , PE and PR was present. Such geometrical mismatch might generate local flow disturbances. Therefore, the PEWT high pressure section was redesigned, which also allowed for improved optical alignment.

The new design features a rectangular cross-sectional shape (see Figs. 8 and 9). In this way, flat optical windows and measuring surface of the pressure transducers (PE, PR) have been mounted flush to the HPS wall, without any geometrical mismatch. In order to minimize the intersections between the main laser beam and the secondary reflections, the two optical windows A_1 and A_3 (see also Fig. 3) have been positioned with the axis mutually parallel and ± 2 mm distant from the centre of the HPS. Doing that, the laser beam can enter the test section through A_1 with an inclination of 7° (see Fig. 9), which prevents any possible optical interference.

The PEWT high-pressure section (HPS) has been also shortened from a length of 1.25 m to about 0.66 m, which speeds up the filling procedure (see Sect. 3) and significantly reduces the gas consumption.

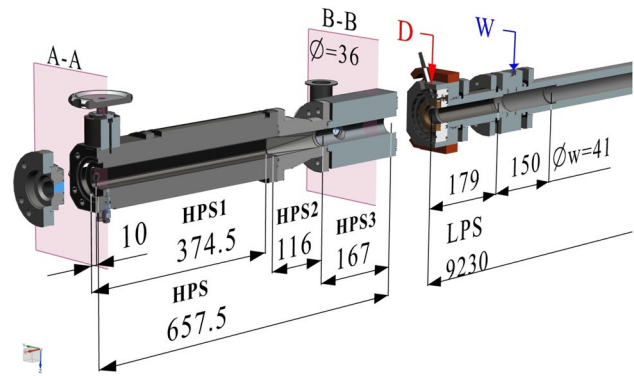


Fig. 8 New HPS: sectioned 3D view of the PEWT (all dimensions in mm). The diaphragm section and the widening (internal diameter $\Phi_w = 41$ mm) are indicated with the letters D and W, respectively. Details on the observation plane (section A-A) are represented in Fig. 9. The rest of the PEWT is characterized by an internal diameter Φ of 36 mm, specified at the plane B-B

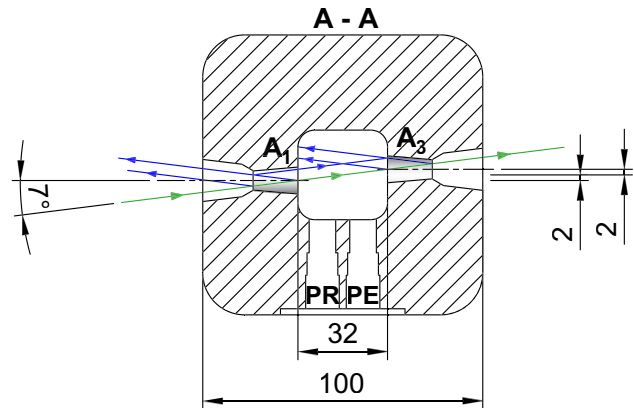


Fig. 9 New rectangular test section side view (dimensions in mm). The flush mounted optical windows (A_1 and A_3) and pressure transducers (PE and PR) can be noted. The laser beam (—) enters the test section from the left side (window A_1) and exits it from the right side (window A_3). The secondary reflections are also represented (—)

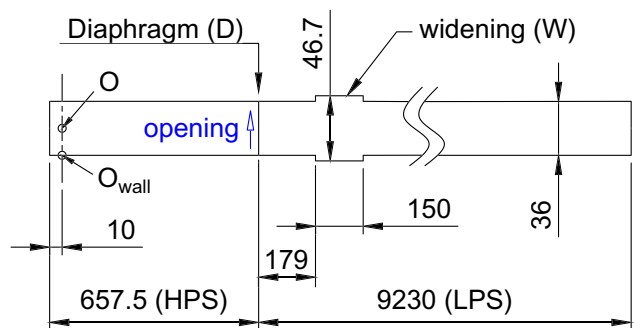


Fig. 10 PEWT 2D geometrical domain (all dimensions in mm). The diaphragm opening direction is indicated with the blue arrow (↑)

Three main parts have been assembled to compose the new HPS: the 0.375 m long *test section* HPS1 (see Fig. 8), which has a square cross area with rounded off corners ($r = 2.67$ mm) and a width of 32 mm (see Fig. 9); the *outlet and vacuum valve section* HPS3 (see Fig. 8) with a circular cross area shape as the LPS, diameter of 36 mm (B-B) and length of 0.167 m; the *transition part* HPS2, having a length of 0.116 m and designed to facilitate a gradual cross-section transition from the circular shape of HPS3 to the square shape of HPS1 (see Fig. 8).

The test section distance from the HPS end-wall has been increased to 10 mm as shown in Fig. 8. In this way, the thermal boundary layer developing from the walls towards the core of the tube does not represent a possible source of disturbance for the last part of the droplet growth process (Luijten 1998; Luo 2004).

The PEWT performances have been examined with two different experimental campaigns. During the first one, the setup has been tested at 4 different pressure ranges with pure helium, analysing

- the added value brought to the measurement quality by the PE with respect to the PR,
- the effect of the coating on the PE measuring surface, applied to protect it from exchange of heat with the gas during the wave experiment,
- the influence of the diaphragm thickness on the pressure profile at the observation point O .

The above mentioned tests have been exploited as reference to design and verify the 2D numerical model described in Sect. 4.

The second experimental campaign has been executed with the purpose of testing the reliability of the modified PEWT setup by performing homogeneous water nucleation and droplet growth experiments. The tested conditions have been 1 MPa and 240 K as nucleation pressure and temperature, respectively. Helium has been chosen as carrier gas, and the results have been compared to the data obtained by Fransen et al. (2015) in the same experimental conditions by means of the previous PEWT version. Details on both test campaigns will be given in Sect. 5.2.

4 2D numerical model

4.1 Computational domain, numerical settings and grid independence study

The PEWT has been modelled in a two-dimensional manner. Details on the geometrical domain are sketched in Fig. 10. The 3D area variation of the PEWT has been modelled in a 2D manner by changing the widening vertical dimension

from 41 to 46.7 mm. This choice allowed to keep the same relative cross-sectional area ratio when passing from the 3D geometry to the 2D model.

The numerical model is based on non-stationary 2D Euler equations:

$$\frac{\partial \mathbf{U}}{\partial t} + \frac{\partial \mathbf{F}}{\partial x} + \frac{\partial \mathbf{G}}{\partial y} = 0, \tag{5}$$

with \mathbf{U} the vector of unknowns and \mathbf{F} and \mathbf{G} convective fluxes in x and y direction, respectively:

$$\mathbf{U} = \begin{pmatrix} \rho \\ \rho u \\ \rho v \\ \rho E \end{pmatrix}; \quad \mathbf{F} = \begin{pmatrix} \rho u \\ \rho u^2 + p \\ \rho uv \\ (\rho E + p)u \end{pmatrix}; \quad \mathbf{G} = \begin{pmatrix} \rho v \\ \rho uv \\ \rho v^2 + p \\ (\rho E + p)v \end{pmatrix}; \tag{6}$$

Equation 6 has been solved in a coupled manner by means of the density-based explicit solution method present in the commercial software ANSYS® Fluent®. The discretization of the convective fluxes \mathbf{F} and \mathbf{G} has been performed by means of the *advection upstream splitting method* (AUSM). For the spacial discretization, the least squares cell-based gradient has been employed, while the third order monotone upstream-centred scheme (MUSCL) has been exploited for the flow discretization. The time integration of the governing equations has been performed by means of a second-order implicit formulation. Helium has been chosen as a simulated gas, and it is assumed to behave as a calorically perfect gas.

In order to minimize the numerical errors due to the grid choice, different mesh sizes have been tested for accuracy and computational time (Δx and Δy both decreasing from 6 mm to 1 mm). Instantaneous opening of the diaphragm has been considered at this stage. A mesh size with $\Delta x = 4$ mm and $\Delta y = 2$ mm has been selected.

Preliminary results of the 2D numerical model are reported in Fig. 11, where the pressure (Fig. 11a) and the temperature (Fig. 11b) profiles in time are compared with the reference experimental results of test 2c* (Table 1). It should be noticed that the shown numerical results are taken at the observation plane wall O_{wall} at this stage. Such a choice has been possible only after the verification of a perfect overlapping for the results taken at O_{wall} and at the observation point O , when the diaphragm opening process is modelled as instantaneous. The simulated pressure and temperature time profiles shown in Fig. 11 differ from the experimental results in three regions: at the first expansion E , at the pulse n_{PEWT} and at the ripple b . Such differences are due to two main reasons. In the first place, the diaphragm opening process has been simulated as instantaneous at this stage, while such assumption is far from the reality. For this reason, the finite diaphragm opening process will be implemented in the 2D numerical model as explained in the next Sect. 4.2. Secondly, the presence of the contact discontinuity, clearly

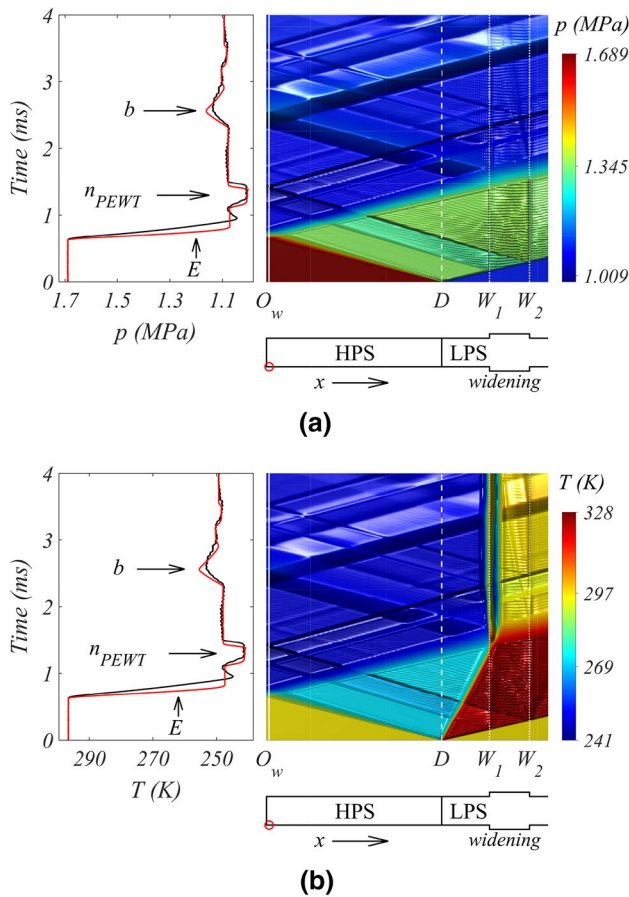


Fig. 11 Pressure (a) and temperature (b) map on the $x - t$ wave diagram. The latter is derived from the 2D numerical tool described in this work, with the represented data taken at the tube wall line in time. The simulated initial conditions are the same as for the test 2c* (Table 1) and the diaphragm opening process is modelled as instantaneous. On the left side of both figures, the pressure (a) and temperature (b) profiles in time (—) are compared with the reference experimental results (—) of test 2c* (Table 1). The simulated profiles are taken at the observation plane wall (O_w), where the transducers are placed (o)

visible on the wave diagram in Fig. 11b, might have interacted with the reflected expansion rE in the proximity of W_1 , contributing with a small overshoot to the ripple b. The latter hypothesis has been verified by simulating the exact same conditions, but without widening in the geometrical domain. A small recompression has been observed, caused by the interaction between the expansion E and the only contact discontinuity cd.

4.2 Modelling of the diaphragm opening process

The 3D opening process of the diaphragm, described in Sect. 3, has been simplified for the present 2D model in

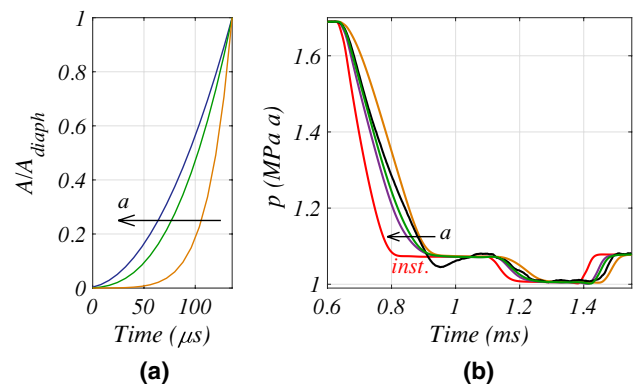


Fig. 12 Parametric study performed with total opening time $t_{diaph} = 136 \mu s$ and varying the exponent a : $a = 1/2$ (—), $a = 3/8$ (—) and $a = 1/8$ (—). In a the different diaphragm opening function $A(t)$ are shown. In b the reference pressure–time profile (test 2c* (Table 1) is compared with the simulated $p(t)$ in O . The pressure profile with instantaneous diaphragm opening (—) is also shown

the following way. It has been assumed that the diaphragm slides away as indicated by the blue arrow sketched in Fig. 10, so that the open area becomes (Arun et al. 2013)

$$\frac{A}{A_{diaph}} = \left(\frac{d}{d_{diaph}} \right)^2 = \left(\frac{t}{t_{diaph}} \right)^{1/a}, \quad (7)$$

with t_{diaph} the total opening time of the diaphragm, A the open area of the diaphragm (d the open diaphragm dimension in the 2D model) at the time t and A_{diaph} the total area of the diaphragm (d_{diaph} the total diaphragm dimension). The duration of each opening time step has been chosen to be 8 ms. The modelled diaphragm has been divided in 18 segments. The initial boundary condition for the whole diaphragm geometry has been set to be a wall, which perfectly separates the HPS from the LPS side. After that, at each consecutive opening time step, the boundary condition for each piece of the diaphragm has been dynamically changed from wall to interior type, starting from the bottom piece of the diaphragm. In this way, with such discrete piece-wise step function, it has been possible to closely approximate the continuous 3D aperture process of the diaphragm.

A parametric study has been performed on a and t_{diaph} . In first instance, the exponent a has been varied from 1/2 to 1/8 (see Fig. 12), with t_{diaph} kept fixed at 136 μs (Looijmans et al. 1993). The best agreement with the reference pressure–time profile of test 2c* (Table 1) has been found for $a=3/8$. Then, t_{diaph} has been varied from 136 to 232 μs (see Fig. 13), with $a=3/8$. A perfect agreement with the experimental reference (test 2c*, Table 1) has been found for $t_{diaph}=184 \mu s$. The 2D numerical model has been also verified with all the other experimental conditions reported in Table 1 as reference and a perfect agreement has been obtained at any condition.

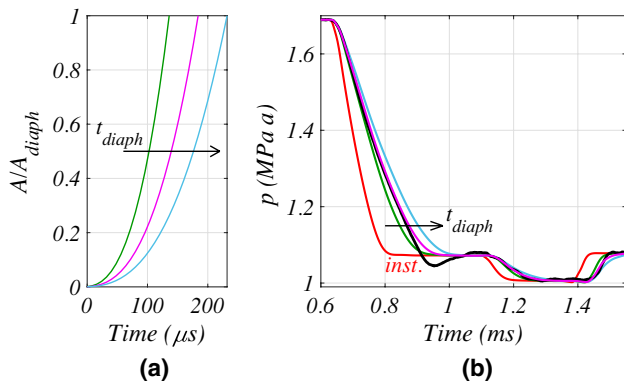


Fig. 13 Parametric study performed with total opening time $a = 3/8$ and varying the t_{diaph} : $t_{diaph} = 136 \mu s$ (—), $t_{diaph} = 184 \mu s$ (—), $t_{diaph} = 232 \mu s$ (—). In **a** the different diaphragm opening function $A(t)$ are shown. In **b** the reference $p(t)$ profile (test $2c^*$, Table 1) is compared with the simulated ones taken in O . The $p(t)$ profile with instantaneous diaphragm opening (—) is also shown

5 Results and discussion

5.1 Numerical results

Now that the complete 2D numerical model has been validated, it is possible to analyse the pressure–time profile at the bottom wall of the observation plane (A-A, see Fig. 8), namely O_{wall} (see Fig. 10), where the pressure transducers are placed. The comparison between the numerical and the reference experimental $p(t)$ and $T(t)$ profiles shows a perfect agreement, when the diaphragm opening process is included in the 2D numerical model (see Fig. 14). It should be also underlined that by modelling the diaphragm opening process the overshoot at the ripple b (see Fig. 11) disappears. This is due to the different position of the contact discontinuity when the reflected expansion wave rE reaches W_1 (see Fig. 14b).

As evident in Fig. 15, the experimental oscillations present at the plateau ($t = 1.5 \div 2.2$ ms) and at the bottom of the pulse ($t = 1.24 \div 1.44$ ms) are also appreciable in the numerical results at O_{wall} . On the contrary, such oscillations appears to be damped at the observation point O for the numerical results. An additional proof of such pressure oscillations is reported in Fig. 16. The position and the shape of the S_2 front wave are highlighted by narrowing the colour-map around the pressure value in O at the beginning of the pulse recompression $t_A = 1.44$ ms (see Fig. 16b). The evolution in time of such wave is shown by considering the time step before ($t_A - 0.004$ ms, see Fig. 16a) and after ($t_A + 0.004$ ms, see Fig. 16c) t_A . Typical oscillation overshoot B and undershoot C of the pressure at O_w are shown in Fig. 16d, e, respectively. In the latter case, the colour-map has been narrowed around the pressure value in O at the time t_B and t_C . In this way, it has been possible to make evident

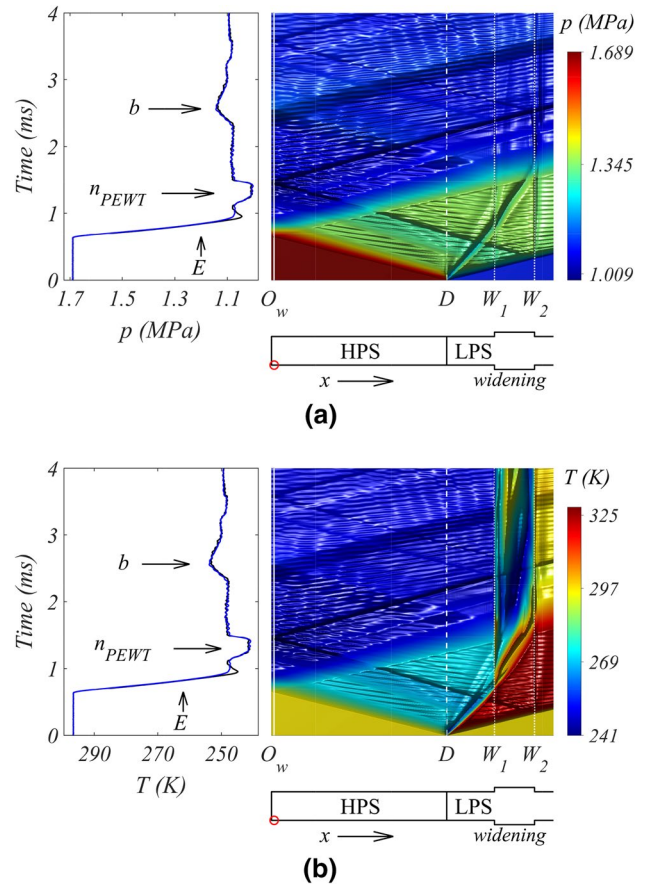


Fig. 14 Pressure **(a)** and temperature **(b)** map on the $x - t$ wave diagram. The latter is derived from the 2D numerical tool described in this work, with the represented data taken at the tube wall line in time. The simulated initial conditions are the same as for the test $2c^*$ (Table 1) and the diaphragm opening process is modelled with $a = 3/8$ and $t_{diaph} = 184 \mu s$. On the left side of both figures, the pressure **(a)** and temperature **(b)** profiles in time (—) are compared with the reference $p(t)$ and $T(t)$ (—) of test $2c^*$ (Table 1). The simulated profiles are taken at the observation plane wall O_w , where the transducers are placed (o)

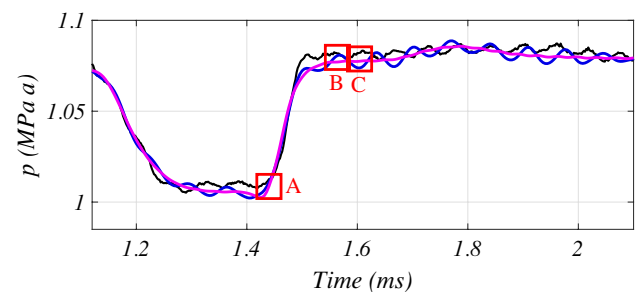


Fig. 15 Pressure–time profile at O (—) and O_{wall} (—) with emphasis on the pulse ($t = 1.24 \div 1.44$ ms) and the plateau ($t = 1.5 \div 2.2$ ms). The experimental pressure measured at O_{wall} for the test condition $2c^*$ (Table 1) is used as reference (—)

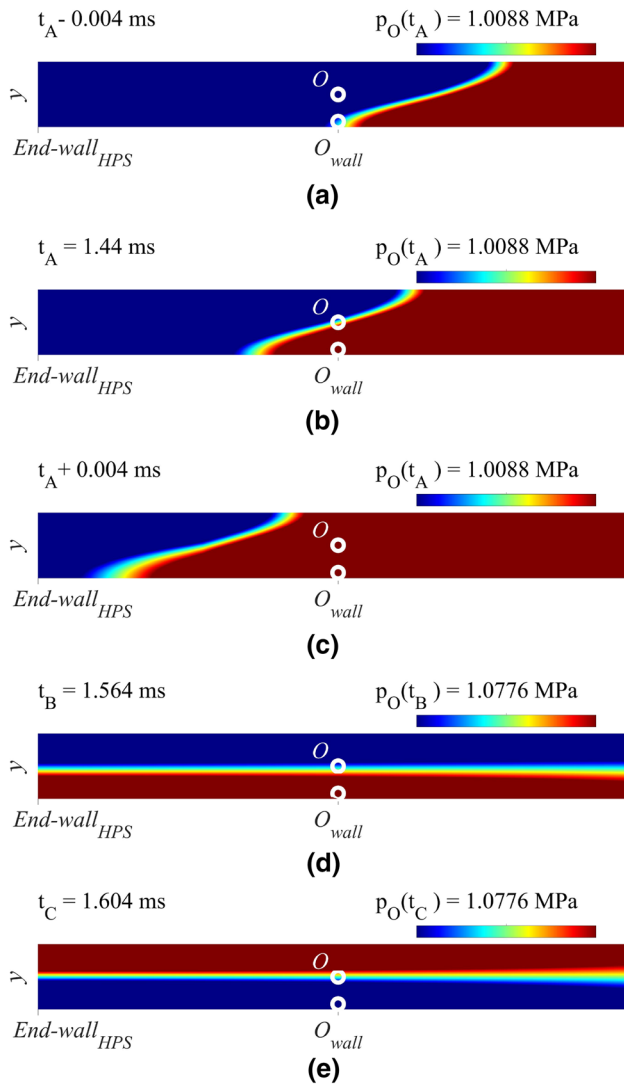


Fig. 16 Simulated pressure colour-map of the HPS for different times: **a** $t_A - 0.004$ ms, **b** $t_A = 1.44$ ms, **c** $t_A + 0.004$ ms, **d** $t_B = 1.564$ ms, **e** $t_C = 1.604$ ms. A, B and C are highlighted in Fig. 15

that the pressure level in O_w alternatively increases and decreases with respect to the pressure level in O . It has been verified that the s-shape of the waves, visible in Fig. 16a–c, appears to be absent for instantaneous opening of the diaphragm. In the latter case, the waves are parallel to the HPS end-wall and the pressure oscillations are completely absent at O_w (see the wave diagrams in Fig. 11a, b). The ripples of the pressure at O_w in time are more evident in Fig. 17. It can be concluded that the pressure oscillations are caused by the 2D diaphragm opening process. Moreover, such disturbances appear to be sensed by the transducers, placed at the bottom wall of the observation plane A-A, while they are strongly muffled at the observation point O . Therefore, it has been proven that no disturbances are expected to affect the flow field at the observation point O .

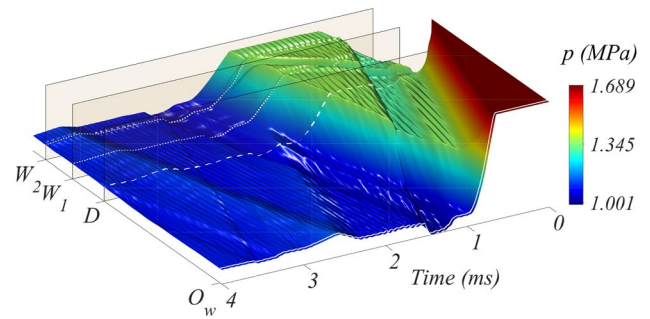


Fig. 17 Pressure map of Fig. 14a in 3D form. The z -direction is representative of the pressure level

5.2 Experimental results

The first experimental campaign with the modified version of the PEWT has been performed by running four sets of dry wave experiments with pure dry helium. Each set of tests corresponds to a different pulse pressure level p_{pulse} . Four levels have been checked. The pressure and temperature values, averaged over the pulse duration Δt_p , are presented in Table 1. The superscript * indicates the tests performed applying the coating layer to the PE transducer (Sect. 3).

The typical temperature profiles with and without coating for PR and PE are shown in Fig. 18. One observes a small but significant difference between the two nucleation temperatures derived from both pressure transducer signals, when the PE is uncoated. It should be noted that a temperature error of 1 K corresponds with a shift in nucleation rate by more than a factor two. The temperature difference disappears when the PE transducer is coated, indicating that the thermal insulation of the coating is effective. Different diaphragm thicknesses have also been tested at 0.5 MPa and 1 MPa, and the results are summarized in Table 1. The 75 μm and 125 μm diaphragms show an influence on the pulse duration Δt_{pulse} , reducing the available time for the mixture to nucleate. This effect points out the importance of using the thinnest diaphragm possible, provided that it stands the pressure difference existing between HPS and LPS at the beginning of the experiment.

A second experimental campaign has been carried out in order to verify the performances of the novel design. Several homogeneous water nucleation experiments have been run with helium as carrier gas and a pulse temperature of about 240 K. Two nucleation pressures have been tested, 1 MPa and 0.1 MPa, at different supersaturation levels. In Fig. 19 the results for such tests are presented in terms of nucleation rate J - supersaturation S data. A detailed overview of the performed nucleation experiments is given in Table 2. For both pressure conditions, a coating layer has been applied to the PE sensing surface and a diaphragm thickness of 50 μm and 40 μm has been found to be the optimal choice at 1

Table 1 Wave experiments overview

Wave Exp.	Diaphragm μs	Δt_{pulse} msec	p_{pulse} MPa	Δp_{pulse} %	T_{pulse} K	ΔT_{pulse} %
1a	50	0.210	0.488	1.20	237.6	0.48
1c *	50	0.210	0.494	0.49	241.5	0.20
1d *	75	0.205	0.492	0.38	241.4	0.15
2a	50	0.215	0.995	1.37	240.1	0.55
2c *	50	0.208	1.012	0.19	241.7	0.08
2d *	75	0.194	1.001	0.27	240.3	0.11
2e *	125	0.180	0.987	0.24	240.2	0.09
3a	125	0.180	1.479	1.25	238.8	0.50
3c *	125	0.180	1.489	0.29	241.9	0.12
4a	125	0.190	1.968	1.17	238.5	0.47
4c *	125	0.185	1.982	0.18	241.9	0.07

The thicknesses of the *diaphragm* and the pulse durations Δt_{pulse} for each experiment are reported. p_{pulse} and T_{pulse} are the PR pressure and temperature averaged during the pulse duration Δt_p , respectively. The $\Delta p_{\text{pulse}} = (p_{\text{pulse,PR}} - p_{\text{pulse,PE}}) * 100 / p_{\text{pulse,PR}}$ and $\Delta T_{\text{pulse}} = (T_{\text{pulse,PR}} - T_{\text{pulse,PE}}) * 100 / T_{\text{pulse,PR}}$ are the relative percentage difference between the PR and the PE measures

The “*” denotes the experiments performed with coated piezoelectric transducer

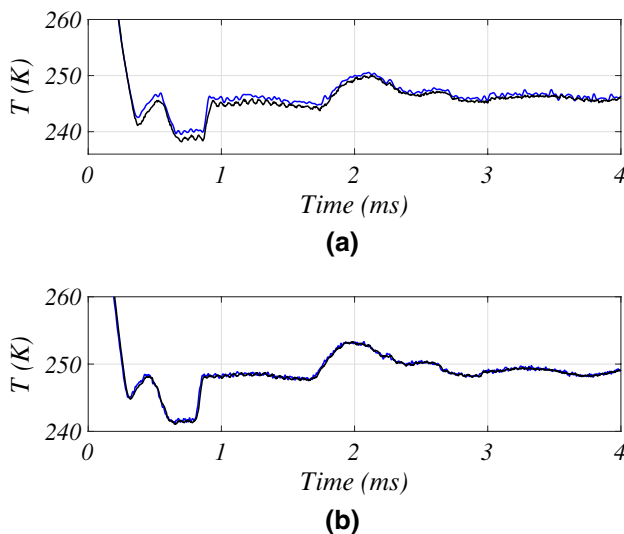


Fig. 18 Temperature profiles at the nucleation pulse obtained from the PR transducer (—) and from the PE transducer (—). In **a** the temperature profiles of the test 2a (Table 1) with uncoated-PE transducer and in **b** the temperature profiles with the test 2c* (Table 1) with coated-PE

MPa and 0.1 MPa, respectively. The measured $J - S$ values are compared with the data obtained by Fransen et al. (2015) in the same conditions as this work, but with the previous version of the PEWT. The main result to be underlined is the substantial agreement with the data of Fransen et al. (2015), which demonstrates the well functioning of the PEWT, in the new version as in the original one of Looijmans et al. (1993).

6 Conclusions

The High pressure section (HPS) of the PEWT for homogeneous condensation experiments has been redesigned. A square-shape cross-section has been chosen for the test section in order to accommodate, without any geometrical mismatch, the pressure transducers (PR and PE) and two of the three optical windows (A_1 and A_3). The HPS has been also halved in length with the scope of a faster experimental procedure and a reduced gas consumption. Two test campaigns have been carried out in order to verify, with the first one, the gasdynamic performances of the modified PEWT and, with the second campaign, the nucleation rate (J) - supersaturation (S) data quality when homogeneous condensation experiments are run. The homogeneous water nucleation data ($J - S$) obtained at 240 K and at two pressure conditions, 1 MPa and 0.1 MPa, in helium with the newly designed PEWT have been shown to be perfectly aligned with previous measurements performed, at the same experimental conditions, by means of the previous version of the PEWT. This means that the modified wave tube is functioning properly. Moreover, it also implies that the quality of the nucleation rate data obtained with the previous version of PEWT is not significantly affected by the slight mismatch of the flat windows and transducers with the circular walls of the previous test section. Both campaigns have demonstrated the combination of piezoresistive (PR) and fast responding coated piezoelectric (PE) transducers to be essential for the purpose of providing a much more accurate measuring of the mixture thermodynamic conditions during the PEWT experiments. The importance of the diaphragm has also been pointed out, proving that the choice of the

Table 2 Experimental data overview of the water nucleation experiments performed with the new version of the PEWT discussed in this work and reported in Fig. 19

Test	p_{sat} (MPa)	T_{sat} (K)	y (ppm)	p_{pulse} (MPa)	T_{pulse} (K)	Δt_{pulse} (ms)	n_d (m ⁻³)	J (m ⁻³ s ⁻¹)	S
1	3.20	296.38	504	1.00949	241.46	0.208	2.18E+11	1.05E+15	12.10
2	3.20	296.68	514	1.00383	241.32	0.202	2.83E+11	1.40E+15	12.39
3	3.20	296.15	494	0.99907	240.41	0.206	4.94E+11	2.40E+15	12.67
4	3.20	296.14	494	0.99285	239.75	0.204	1.26E+12	6.17E+15	13.18
5	3.20	296.64	509	0.99512	240.31	0.206	1.30E+12	6.32E+15	13.09
6	2.575	291.11	448	0.98943	239.85	0.200	4.60E+10	2.30E+14	11.83
7	2.575	291.08	529	0.99342	239.87	0.204	7.88E+12	3.86E+16	13.99
8	2.575	291.12	489	0.98796	240.75	0.204	1.18E+11	5.77E+14	12.09
9	2.575	291.07	488	0.98861	239.89	0.202	8.69E+11	4.30E+15	12.83
10	2.558	291.08	488	0.99004	240.37	0.200	2.03E+11	1.02E+15	12.43
11	2.575	291.08	447	0.99771	240.76	0.206	1.24E+10	6.01E+13	11.15
12	2.575	291.06	516	0.98930	239.75	0.210	4.67E+12	2.22E+16	13.71
13	0.3	291.02	4803	0.10405	239.92	0.142	4.29E+11	3.02E+15	13.37
14	0.3	291.03	4797	0.10453	240.67	0.148	9.71E+10	6.56E+14	12.72
15	0.3	291.02	4795	0.10317	239.80	0.146	3.82E+11	2.61E+15	13.34
16	0.3	291.02	5313	0.10494	241.39	0.152	4.80E+11	3.16E+15	13.44
17	0.3	291.01	5188	0.10269	239.22	0.148	1.37E+13	9.26E+16	14.95
18	0.3	291.02	5311	0.10247	239.22	0.144	1.43E+13	9.95E+16	15.27
19	0.3	291.02	5310	0.10252	239.50	0.142	9.65E+12	6.80E+16	14.99
20	0.3	291.01	4884	0.10424	239.47	0.134	8.69E+11	6.48E+15	14.05
21	0.3	291.01	4889	0.10432	239.90	0.142	8.30E+11	5.85E+15	13.66
22	0.4	291.01	4243	0.10397	239.52	0.138	1.28E+10	9.24E+13	12.14
23	0.4	291.01	4177	0.10387	239.20	0.136	2.14E+10	1.57E+14	12.21

The subscript “sat” denotes the saturation quantities, and the subscript “pulse” stands for the pulse quantities

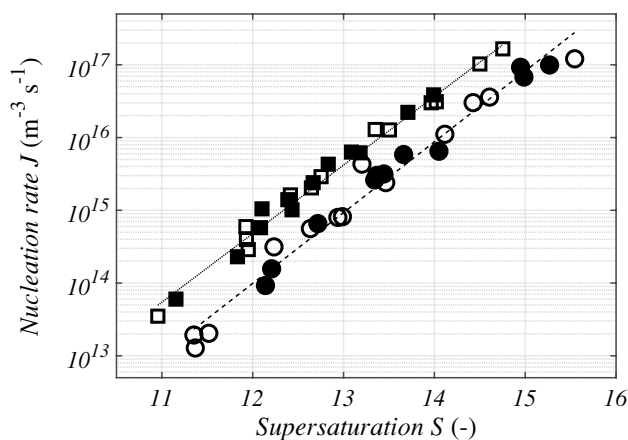


Fig. 19 Experimental data overview of the water nucleation rates J in function of the supersaturation S at 240 K in helium. The data obtained with the new version of the PEWT at 1 MPa (■) and 0.1 MPa (●) are presented. A detailed overview is reported in Table 2. The data of Fransen et al. (2015) at 1 MPa (□) and 0.1 MPa (○), with the previous PEWT version, are also shown for comparison. The two trend lines at 1 MPa (···) and 0.1 MPa (---) have the only purpose of guiding the eye

thinnest diaphragm thickness possible is crucial to minimize the diaphragm opening process intrusiveness during the experiments. Additionally, a 2D numerical model has been successfully developed for the PEWT, representing a powerful support for the design of the forthcoming experiments. Such tool has been shown to correctly predict all the gasdynamic features of the PEWT, including the opening process and the total opening time of the diaphragm and it has been possible to exclude the presence of any disturbance on the flow field at the observation point.

Acknowledgements The discussions with dr. J. Hrubý (Academy of Science of the Czech Republic) are gratefully acknowledged. The authors wish to thank J.G.H. van Griensven, H.P.J. Vliegen, J.M. de Hullu and the technical staff of the Energy Technology Group (Mechanical Engineering Department - Eindhoven University of Technology) for their support and helpfulness.

Open Access This article is licensed under a Creative Commons Attribution 4.0 International License, which permits use, sharing, adaptation, distribution and reproduction in any medium or format, as long as you give appropriate credit to the original author(s) and the source, provide a link to the Creative Commons licence, and indicate if changes were made. The images or other third party material in this article are included in the article's Creative Commons licence, unless indicated otherwise in a credit line to the material. If material is not included in the article's Creative Commons licence and your intended use is not

permitted by statutory regulation or exceeds the permitted use, you will need to obtain permission directly from the copyright holder. To view a copy of this licence, visit <http://creativecommons.org/licenses/by/4.0/>.

Appendix: Definition of the supersaturation

The supersaturation can be defined for a non-ideal vapour–gas mixture as (Vehkamäki 2006; Holten et al. 2016)

$$S_i = \exp \left[\frac{\mu_i^v(p, T, y_i) - \mu_i^v(p, T, y_{i,eq})}{kT} \right] \tag{8}$$

and quantifies, relatively to the mixture component i , the deviation of the current state from the corresponding (same p and T) phase equilibrium. In Eq. 8, the term $\mu_i^v(p, T, y_i)$ is the chemical potential of the i -component in the vapour state v at the system conditions p and T , while $\mu_i^v(p, T, y_{i,eq})$ is the chemical potential of the same component, but in the vapour–liquid equilibrium at the same mixture conditions p and T . In case of non-ideal vapour–gas mixture, the exponent of Eq. 8 is defined as

$$\frac{\mu_i^v - \mu_{i,eq}^v}{kT} = \log \left(\frac{f_i}{f_{i,eq}} \right), \tag{9}$$

with f_i and $f_{i,eq}$ the fugacities of the i -component at the vapour state and at the equilibrium state, respectively. In function of the activity f , the fugacity coefficient ϕ can be expressed in a general manner as

$$\phi = \frac{f_i}{y_i p}. \tag{10}$$

Moreover, the approximation

$$\phi_i \approx \phi_{i,eq}, \tag{11}$$

can be made for the present application since y is appreciably small (~ 500 ppm) and, therefore, almost all molecular interaction can be assumed to take place between the vapour and the gas molecules (dilute gas). In consideration of Eqs. (8, 9, 10 and 11), the supersaturation can now be expressed as

$$S_i = \frac{\phi_i y_i}{\phi_{i,eq} y_{i,eq}} \approx \frac{y_i}{y_{i,eq}} = \frac{y_i p}{f_e p_{i,s}} \tag{12}$$

with the enhancement factor f_e , defined as

$$f_e = \frac{y_{i,eq} p}{p_{i,s}} = \frac{\phi_{i,s}}{\phi_{i,eq}} \exp \left(\int_{p_{i,s}}^p v^l dp \right). \tag{13}$$

Such factor takes into account two important contributions: the pressure effects on the equilibrium phase by means of the Poynting correction ($\int_{p_{i,s}}^p v^l dp$) and the effect of the non-ideal gas behaviour with the ratio $\phi_{i,s}/\phi_{i,eq}$. In the case of ideal vapour–gas mixtures, $f_e \approx 1$ and the supersaturation definition (Eq. 12) simplifies as follows

$$S_i = \frac{y_i p}{p_{i,s}} = \frac{p_{i,v}}{p_{i,s}}. \tag{14}$$

with $p_{i,v} = y_i p$ the partial vapour pressure of the mixture component i .

References

Allard EF, Kassner JL (1965) New cloud-chamber method for the determination of homogeneous nucleation rates. *J Chem Phys* 42(4):1401–1405. <https://doi.org/10.1063/1.1696129>

Arun KR, Kim HD, Setoguchi T (2013) Effect of finite diaphragm rupture process on microshock tube flows. *J Fluids Eng.* doi 10(1115/1):4024196

Fransen MALJ, Sachteleben E, Hrubý J, Smeulders DMJ (2014) On the growth of homogeneously nucleated water droplets in nitrogen: an experimental study. *Exp Fluids* 55(7):1780. <https://doi.org/10.1007/s00348-014-1780-y>

Fransen MALJ, Hrubý J, Smeulders DMJ, van Dongen MEH (2015) On the effect of pressure and carrier gas on homogeneous water nucleation. *J Chem Phys* 142(16):164307. <https://doi.org/10.1063/1.4919249>

Holten V, Labetski DG, van Dongen MEH (2005) Homogeneous nucleation of water between 200 and 240 K: new wave tube data and estimation of the Tolman length. *J Chem Phys* 123(10):104505. <https://doi.org/10.1063/1.2018638>

Holten V, Hrubý J, van Dongen M, Smeulders D (2016) Comment on “unraveling the ‘pressure effect’ in nucleation”. [arXiv:160309583](https://arxiv.org/abs/160309583)

Hrubý J (1999) New mixture-preparation device for investigation of nucleation and droplet growth in natural gas-like systems. Technical report R-1489-D, Eindhoven University of Technology

Kalikmanov V, Betting M, Bruining J, Smeulders D (2007) New developments in nucleation theory and their impact on natural gas separation. In: Proceedings of the SPE annual technical conference and exhibition, 11–14 November 2007, Anaheim, California, pp 11–14

Looijmans KNH, van Dongen MEH (1997) A pulse-expansion wave tube for nucleation studies at high pressures. *Exp Fluids* 23(1):54–63. <https://doi.org/10.1007/s003480050086>

Looijmans KNH, Kriesels PC, van Dongen MEH (1993) Gasdynamic aspects of a modified expansion-shock tube for nucleation and condensation studies. *Exp Fluids* 15(1):61–64. <https://doi.org/10.1007/BF00195596>

Luijten CCM (1998) Nucleation and droplet growth at high pressure. Ph.D. thesis, Department of Applied Physics, pp 78–80. <https://doi.org/10.6100/IR516103>

Luo X (2004) Unsteady flows with phase transition. Ph.D. thesis, Department of Applied Physics, pp 64–66. <https://doi.org/10.6100/IR576382>

Peters F (1983) A new method to measure homogeneous nucleation rates in shock tubes. *Exp Fluids* 1(3):143–148. <https://doi.org/10.1007/BF00272013>

Strey R, Wagner P, Viisanen Y (1994) The problem of measuring homogeneous nucleation rates and the molecular contents of

- nuclei: progress in the form of nucleation pulse measurements. *J Phys Chem* 98(32):7748–7758
- Vehkamäki H (2006) Classical nucleation theory in multicomponent systems. Springer, Berlin
- Wagner PE (1985) A constant-angle Mie scattering method (CAMS) for investigation of particle formation processes. *J Colloid Interface Sci* 105(2):456–467
- Wagner PE, Strey R (1981) Homogeneous nucleation rates of water vapor measured in a two-piston expansion chamber. *J Phys Chem* 85(18):2694–2698. <https://doi.org/10.1021/j150618a026>
- Wyslouzil BE, Wölk J (2016) Overview: homogeneous nucleation from the vapor phase—the experimental science. *J Chem Phys* 145(21):211702. <https://doi.org/10.1063/1.4962283>

Publisher's Note Springer Nature remains neutral with regard to jurisdictional claims in published maps and institutional affiliations.